Flight-Dynamics and Flutter Modeling and Analysis of a Flexible Flying-Wing Drone - Invited

Dr. David K. Schmidt[*]
University of Colorado-Colorado Springs
Colorado Springs, CO 80918

Wei Zhao[†] and Dr. Rakesh K. Kapania[‡]
Virginia Polytechnic Institute and State University
Blacksburg, VA 24061

Abstract

A relatively low-order, linear dynamic model is developed for the longitudinal flight-dynamics analysis of a flexible, flying-wing drone, and model-based results are compared to results from flight test as well as from several other high-order models. The model includes the dynamics of the coupled rigid-body and elastic degrees of freedom, and the subject vehicle is designed to flutter within its flight envelope. The vehicle of interest is a 14.7-pound unmanned, flying-wing aircraft with a wingspan of 10 ft. In the modeling, the rigid-body degrees of freedom are defined in terms of motion of a body-referenced coordinate frame, as required for flight-dynamics analysis. As a result, the state variables corresponding to the rigid-body degrees of freedom are identical to those used in modeling a rigid vehicle. Both body-freedom and bending-torsion flutter conditions are indicated by the model, and it is shown that the transient response, flutter speeds, frequencies, and genesis vibration modes suggested by this low-order model agree very well with NASTRAN and other higher-order, model-based predictions and flight-test results. The longitudinal dynamics of this flexible vehicle are characterized by a slightly unstable phugoid mode, a well-damped, pitch-dominated, elastic-short-period mode, and the stable or unstable aeroelastic modes. A classical, rigid-body, short-period mode does not exist, and the elastic-short-period and first two aeroelastic modes involve significant coupling between the rigid-body and elastic degrees of freedom.

I. Introduction

As part of a multidisciplinary, multi-organization research project, we seek to develop a model for the dynamic analysis of a flexible, flying-wing drone. Since the vehicle is being developed for aeroelastic research, this model must capture the dynamics of both the rigid-body and elastic degrees of freedom (DOFs), including critical flutter conditions. Such models are usually called n-degree-of-freedom (nDOF) models. This work is an extension of that reported in [1], and the vehicle considered here, as well as the analysis, is similar but not identical to that addressed in the reference. In this investigation we will develop the nDOF model from first principles, use MSN/NASTRAN [2] to obtain the solution to the free-vibration problem for the structure, generate the aerodynamic data using the vortex-lattice method (VLM), discuss model updates based on parameters identified during flight tests, and compare the model-based flutter predictions to those obtained using several other modeling techniques considered to be of high fidelity.

We will focus here on a novel modeling methodology that can yield accurate yet relatively simple dynamic models that provide valuable insight into the vehicle's dynamics, and can be available early in the design-cycle, as opposed to later, which is frequently the case for NDOF models. The dynamics so modeled will also be expressed in a body-reference coordinate frame, rather than inertial, to allow for flight-dynamics analysis and control-law design.

[*] Professor Emeritus, Department of Mechanical and Aerospace Engineering, Fellow, AIAA
[†] PhD Student, Department of Aerospace and Ocean Engineering, Student Member, AIAA
[‡] Mitchell Professor, Department of Aerospace and Ocean Engineering, Associate Fellow, AIAA

American Institute of Aeronautics and Astronautics

We also require that parameters in our model can be easily updated, as more accurate aerodynamic data become available.

II. The Flight-Dynamics (FD) Modeling Methodology

We will utilize a modeling approach that fundamentally differs from that frequently taken in developing aeroelastic models (c.f., [2]). Sophisticated modeling techniques have been developed within the aeroelasticity/structural-dynamics communities for flutter and loads predictions in aircraft design, and these tools and methodologies have been tailored and optimized to accomplish these specific objectives. With coupling between the rigid-body and elastic degrees of freedom now becoming more important, these traditional flutter-analysis tools are being extended in an attempt to also capture the rigid-body DOFs. In contrast, one may view our approach as beginning with a rigid-body flight-dynamics model and extending it to include the elastic degrees of freedom.

Major differences exist between flutter-modeling approaches and models developed for flight-dynamics analysis. For example flutter models typically exclude the surge-translation rigid-body degree of freedom, hence eliminating the phugoid mode. But the primary differences between the two modeling approaches involve the coordinate frames used in deriving the equations of motion, and the model format. In flutter models all the DOFs, as well as aerodynamic forces and moments, are defined in the inertial reference frame, while in flight-dynamics modeling the motion variables, forces, and moments are always defined in a body-reference frame. The latter approach, for example, yields time-invariant vehicle-mass properties (for rigid vehicles) and is compatible with on-board sensor measurements employed in the flight-control systems as well as piloted simulations.

The modeling approach to be utilized, as discussed in [3] and depicted in Fig. 1, is consistent with conventional aeroelastic theory [4] and develops an integrated nDOF model using a body-referenced frame from the outset. The dashed box in Fig. 1 indicates that unsteady aerodynamics may or may not be specifically included in the modeling. Finally, to meet the second goal of obtaining dynamic models earlier in the design cycle, a simpler FEM beam-element model may be used to obtain the vibration solution, a variety of methods are used to estimate the rigid-body stability derivatives, and quasi-steady or unsteady strip-theoretic techniques [5], also implemented in MATLAB[®] scripts, are applied to estimate aeroelastic coefficients analogous to the stability derivatives used in rigid-vehicle flight-mechanics models.
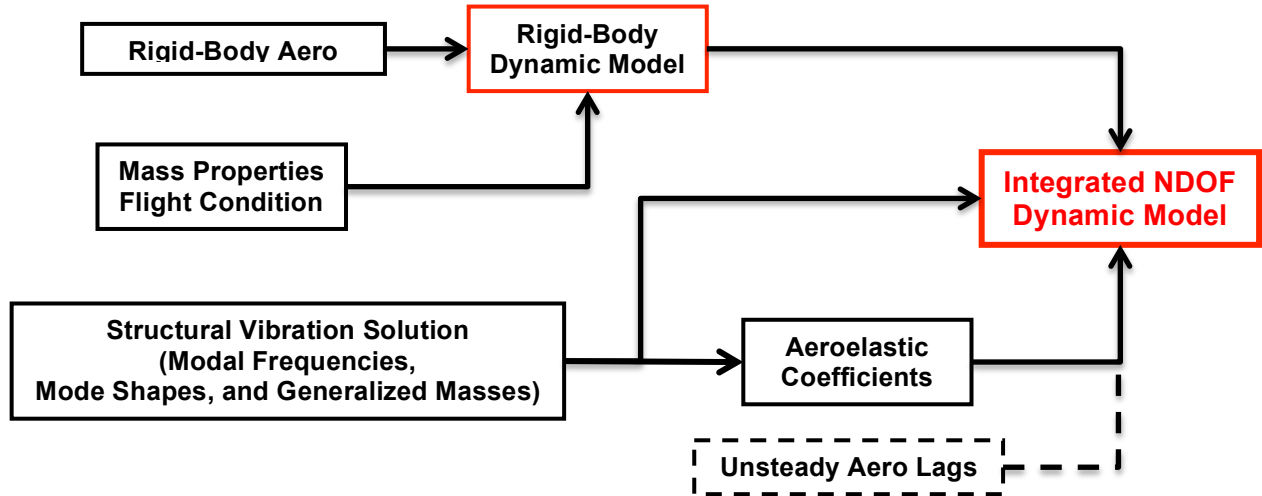

Figure 1, Modeling Methodology

A. The Equations of Motion and Mean Axes

Following the presentation from [6], and to aid in the discussions to follow, let us review the derivation of the equations of motion used by several authors (c.f., [7-9]). Let the inertial position of a point P on a deformable elastic structure be expressed as

$$\mathbf{p}' = \mathbf{p}_{cm} + \mathbf{p} = \mathbf{p}_{cm} + \mathbf{p}_{RB} + \mathbf{d}_E \qquad \qquad 1$$

where $\mathbf{p}_{cm}$ is the inertial position of the instantaneous center of mass of the body, $\mathbf{p}_{RB}$ is the position of P relative to the center of mass in the undeformed body, and $\mathbf{d}_E$ is the displacement of P due to elastic deformation. We also

introduce a body-referenced frame B, as yet not completely defined, and so the velocity of P with respect to the inertial frame I may be expressed as

$$\frac{d\mathbf{p}'}{dt}\bigg|_I = \mathbf{V}_{cm} + \frac{d\mathbf{p}}{dt}\bigg|_I = \mathbf{V}_{cm} + \frac{d\mathbf{p}}{dt}\bigg|_B + \boldsymbol{\omega}_{B,I} \times \mathbf{p} = \mathbf{V}_{cm} + \boldsymbol{\omega}_{B,I} \times \left(\mathbf{p}_{RB} + \mathbf{d}_E\right) + \frac{d\mathbf{d}_E}{dt}\bigg|_B \qquad 2$$

where $\mathbf{V}_{cm}$ is the inertial velocity of the center of mass and $\boldsymbol{\omega}_{B,I}$ is the angular velocity of the body frame with respect to inertial.

Now the body's kinetic energy T may be expressed as

$$T = \frac{1}{2}m\mathbf{V}_{cm}\bullet\mathbf{V}_{cm} + \frac{1}{2}\boldsymbol{\omega}_{B,I}^T\mathbf{J}\boldsymbol{\omega}_{B,I} + \frac{1}{2}\int_{Vol}\frac{d\mathbf{d}_E}{dt}|_B\bullet\frac{d\mathbf{d}_E}{dt}|_B\,\rho_B\,dV + \mathbf{V}_{cm}\bullet\int_{Vol}\frac{d\mathbf{d}_E}{dt}|_B\rho_B\,dV$$

$$+\,\mathbf{V}_{cm}\bullet\int_{Vol}\left(\boldsymbol{\omega}_{B,I}\times\left(\mathbf{p}_{RB}+\mathbf{d}_E\right)\right)\rho_B\,dV + \boldsymbol{\omega}_{B,I}\bullet\int_{Vol}\left(\left(\mathbf{p}_{RB}+\mathbf{d}_E\right)\times\frac{d\mathbf{d}_E}{dt}|_B\right)\rho_B\,dV \qquad 3$$

where ρ_B is the mass-density distribution of the body, assumed time independent, m is the constant total mass of the body, and $\mathbf{J}$ is its instantaneous inertia tensor (including the geometric effects of elastic deformation). From the excellent presentation in [10] we write

$$\frac{1}{2}\boldsymbol{\omega}_{B,I}^T\mathbf{J}\boldsymbol{\omega}_{B,I} = \frac{1}{2}\boldsymbol{\omega}_{B,I}^T\left[\mathbf{J}_0 + \Delta\mathbf{J} + \Delta^2\mathbf{J}\right]\boldsymbol{\omega}_{B,I}$$

$$\left[\mathbf{J}_0\right] \triangleq \left[\int_{Vol}\tilde{\mathbf{p}}_{RB}\tilde{\mathbf{p}}_{RB}^T\rho_B\,dV\right]$$

$$\left[\Delta\mathbf{J}\right] \triangleq \left[\int_{Vol}\left(\tilde{\mathbf{p}}_{RB}\tilde{\mathbf{d}}_E^T + \tilde{\mathbf{d}}_E\tilde{\mathbf{p}}_{RB}^T\right)\rho_B\,dV\right] \qquad 4$$

$$\left[\Delta^2\mathbf{J}\right] \triangleq \left[\int_{Vol}\tilde{\mathbf{d}}_E\tilde{\mathbf{d}}_E^T\rho_B\,dV\right]$$

where in the above, skew-symmetric matrices $(\tilde{\bullet})$ are introduced to write the vector cross products.

In preparation for the application of the Method of Assumed Modes or Rayleigh-Ritz, we now introduce spatially-dependent shape functions $\boldsymbol{\phi}_i(x,y,z)$ and time-dependent participation functions $\eta_i(t)$ to discretize the structure and to describe the elastic deformation of the body. Furthermore, assume that the solution to the free-vibration problem for the deformable body is known, so the free-vibration frequencies ω_{Vi}, generalized masses M_{Vii}, and the normal mode shapes $\boldsymbol{\phi}_{Vi}$ are known. These mode shapes, therefore, describe the elastic deformation of the structure, relative to the coordinate frame defined (explicitly or implicitly) as part of the solution to the free-vibration problem. Now select these normal mode shapes as the shape functions defined above. So the elastic deformation under free vibration, expressed in terms if these selected shape functions, are

$$\mathbf{d}_{EV}\left(x,y,z,t\right) = \sum_{i=1}^{\infty}\boldsymbol{\phi}_{Vi}(x,y,z)\eta_{Vi}(t)$$

and $\qquad\qquad\qquad\qquad\qquad\qquad\qquad\qquad\qquad\qquad\qquad\qquad\qquad\qquad\qquad 5$

$$\frac{d\mathbf{d}_{EV}\left(x,y,z,t\right)}{dt}\bigg|_B = \sum_{i=1}^{n}\boldsymbol{\phi}_{Vi}(x,y,z)\dot{\eta}_{Vi}(t)$$

where η_{Vi} is the i'th time-dependent participation coefficient, or modal coordinate, associated with the free-vibration solution.

Key is the fact that the constraints imposed on the deformations $\mathbf{d}_{EV}$ of a body under free vibration include (e.g., Refs, 3,4,8,9,10)

$$\int_{Vol}\mathbf{d}_{EV}\rho_B\,dV = \int_{Vol}\mathbf{p}_{RB}\times\mathbf{d}_{EV}\rho_B\,dV = \mathbf{0}$$

or $\qquad\qquad\qquad\qquad\qquad\qquad\qquad\qquad\qquad\qquad\qquad\qquad\qquad\qquad\qquad 6$

$$\sum_{i=1}^{\infty}\left(\int_{Vol}\boldsymbol{\phi}_{Vi}\rho_B\,dV\right)\eta_{vi} = \sum_{i=1}^{\infty}\left(\int_{Vol}\mathbf{p}_{RB}\times\boldsymbol{\phi}_{Vi}\rho_B\,dV\right)\eta_{Vi} = \mathbf{0}$$

which further imply that

$$\int_{Vol} \boldsymbol{\phi}_{V\,i}\rho_B\,dV = \int_{Vol} \mathbf{p}_{RB}\times\boldsymbol{\phi}_{V\,i}\rho_B\,dV = \mathbf{0} \quad \text{for all } i \tag{7}$$

and that

$$\int_{Vol} \left.\frac{d\mathbf{d}_{EV}}{dt}\right|_B \rho_B\,dV = \int_{Vol} \mathbf{p}_{RB}\times\left.\frac{d\mathbf{d}_{EV}}{dt}\right|_B \rho_B\,dV = \mathbf{0} \tag{8}$$

Equations 6 and 7 are recognized as the well-known conditions of mass orthogonality between the free-vibration (normal) modes and the rigid-body translational and rotational modes of motion, or the so-called "practical mean-axis constraints" [8]. To simplify notation, we will hereafter drop the subscript "V" associated with the elastic deformation, as well as the shape and participation functions, and refer to them as simply $\mathbf{d}_E$, ϕ_i and η_i, but the shape functions will always be taken to be the free-vibration mode shapes.

In terms of our shape functions, the first-and second order changes in the inertia tensor in Eqn. 4. become

$$\left[\Delta\mathbf{J}\right] = \sum_{i=1}^{n}\left[\int_{Vol}\left(\tilde{\mathbf{p}}_{RB}\tilde{\boldsymbol{\phi}}_i^T + \tilde{\boldsymbol{\phi}}_i\tilde{\mathbf{p}}_{RB}^T\right)\rho_B dV\right]\eta_i \triangleq \sum_{i=1}^{n}\left[\Delta J_i\right]\eta_i(t)$$

$$\left[\Delta^2\mathbf{J}\right] = \sum_{i=1}^{n}\left(\sum_{j=1}^{n}\left[\int_{Vol}\tilde{\boldsymbol{\phi}}_i\tilde{\boldsymbol{\phi}}_j^T\rho_B dV\right]\eta_i\eta_j\right) \triangleq \sum_{i=1}^{n}\left(\sum_{j=1}^{n}\left[\Delta^2 J_{i,j}\right]\eta_i\eta_j(t)\right) \tag{9}$$

We can also re-write several of the other terms in the kinetic energy in Eqn. 3. The third term in this equation becomes

$$\frac{1}{2}\int_{Vol}\left(\sum_{i=1}^{n}\left.\frac{d\mathbf{d}_{E_i}}{dt}\right|_B\right)\cdot\left(\sum_{j=1}^{n}\left.\frac{d\mathbf{d}_{E_j}}{dt}\right|_B\right)\rho_B dV = \frac{1}{2}\sum_{i=1}^{n}\left(\sum_{j=1}^{n}\left[\int_{Vol}\left(\boldsymbol{\phi}_i\cdot\boldsymbol{\phi}_j\right)\rho_B dV\right]\dot{\eta}_i\dot{\eta}_j\right) \triangleq \frac{1}{2}\dot{\boldsymbol{\eta}}^T\mathbf{M}\dot{\boldsymbol{\eta}} \tag{10}$$

where $\mathbf{M}$ (= $\mathbf{M}_V$) is recognized as the generalized mass matrix from the free-vibration solution, with elements $M_{i,j}$. Invoking Eqns. 6-8, and requiring the origin of the body-reference frame to be coincident with the body's instantaneous center of mass, the first mass moment of the body about it's cm, along with the fourth and fifth terms in the kinetic energy all vanish, while the sixth term reduces to

$$\boldsymbol{\omega}_{B,I}\cdot\sum_{i=1}^{n}\left(\sum_{j=1}^{n}\left(\mathbf{h}_{i,j}\right)\eta_i\dot{\eta}_j\right), \qquad \mathbf{h}_{i,j} \triangleq \int_{Vol}\left(\boldsymbol{\phi}_i\times\boldsymbol{\phi}_j\right)\rho_B dV \tag{11}$$

Therefore, the kinetic energy becomes more simply

$$T_{MA} = \frac{1}{2}m\mathbf{V}_{cm}\cdot\mathbf{V}_{cm} + \frac{1}{2}\boldsymbol{\omega}_{B,I}^T\left[\mathbf{J}_0 + \Delta\mathbf{J} + \Delta^2\mathbf{J}\right]\boldsymbol{\omega}_{B,I} + \frac{1}{2}\dot{\boldsymbol{\eta}}^T\mathbf{M}\dot{\boldsymbol{\eta}} + \boldsymbol{\omega}_{B,I}\cdot\sum_{i=1}^{n}\left(\sum_{j=1}^{n}\left(\mathbf{h}_{i,j}\right)\eta_i\dot{\eta}_j\right) \tag{12}$$

in which the terms are recognized, respectively, as kinetic energy from translation and rotation of the rigid-body subsystem, deformation of the elastic subsystem, and the last involving inertial coupling among the rigid-body and elastic degrees of freedom.

We now define a Reference Coordinate Frame (RCF) in terms of the "global coordinates" defined in the solution to the free-vibration problem, and this coordinate frame is well defined in the undeformed body. The RCF is parallel to the vibration-solution "global" coordinate frame, its origin is at the center of mass of the undeformed body, and since under free vibration there are no external forces it remains fixed in inertial space. Furthermore, translations and rotations of this RCF describe the rigid-body modes of motion for the body, and elastic displacements are defined relative to this frame. So the frame is not attached to any material point on the body, and this RCF constitutes a <u>mean-axis system</u>.

As indicated in [7-9], for example, mean axes are defined as an orthogonal axis system carried in the body having its origin at the instantaneous center of mass of the deformable body and oriented such that Eqns. 6 are always satisfied. And we saw that the free-vibration mode shapes also satisfy the equivalent mean-axis conditions of Eqns. 8. Unlike with rigid bodies, for which the body-fixed axes must only have their origin at the center of mass, the mean axes of flexible bodies must have both their origin at the center of mass and a (directly or indirectly) specified orientation with respect to the body. In words familiar in flight mechanics, a "structural reference axis" must be used.

The equations of motion may now be obtained through application of Lagrange's Equation expressed in terms of "quasi-coordinates," as in [10], for example. The above expression for kinetic energy, Eqn. 12, may be utilized, along with the potential energy due to gravitational attraction under a uniform gravitational field given by

$$U_g = -m\mathbf{g} \bullet \mathbf{p}_{cm} \qquad\qquad 13$$

where $\mathbf{p}_{cm}$ is the inertial position of the center of mass (Eqns. 1). Since our shape functions are taken to be the free-vibration mode shapes, the strain energy in the deformed structure may be expressed in terms of these normal modes, the generalized masses, and the vibration frequencies as

$$U_S = \frac{1}{2}\sum_{i=1}^{\infty} M_{Vii}\omega_{Vi}^2\eta_{Vi}^2 \qquad\qquad 14$$

(although some authors consider higher-order expressions for strain energy.) Note that Eqn. 14 may also be represented in terms of the stiffness matrix $\mathbf{K}$, arising from the free-vibration solution. And again, the free-vibration mode shapes must be selected as the Raleigh-Ritz shape functions.

The resulting non-linear vector equations of motion under this mean-axis formulation are

$$\boxed{m\frac{d\mathbf{V}_{cm}}{dt}\bigg|_B + m\left(\boldsymbol{\omega}_{B,I}\times\mathbf{V}_{cm}\right) = m\mathbf{g} + \mathbf{F}}$$

$$\boxed{[\mathbf{J}]\frac{d\boldsymbol{\omega}_{B,I}}{dt}\bigg|_B + \boldsymbol{\omega}_{B,I}\times[\mathbf{J}]\boldsymbol{\omega}_{B,I}} + \left[\frac{d\mathbf{J}}{dt}\bigg|_B\right]\boldsymbol{\omega}_{B,I} + \mathbf{h}_{i,j}\left(\dot{\eta}_i\dot{\eta}_j + \eta_i\ddot{\eta}_j\right) + \boldsymbol{\omega}_{B,I}\times\mathbf{h}_{i,j}\eta_i\dot{\eta}_j = \boxed{\mathbf{L}} \qquad 15$$

$$\sum_{j=1}^{n}\left(\boxed{M_{ij}\ddot{\eta}_j + K_{i,j}\eta_j} - \frac{d\boldsymbol{\omega}_{B,I}}{dt}\bigg|_B\bullet\mathbf{h}_{i,j}\eta_j - 2\boldsymbol{\omega}_{B,I}\bullet\mathbf{h}_{i,j}\dot{\eta}_j\right) - \frac{1}{2}\boldsymbol{\omega}_{B,I}^T\left[\overline{\Delta\mathbf{J}}\right]\boldsymbol{\omega}_{B,I} = \boxed{Q_i}, \quad i = 1\cdots n$$

and the inertial position of any point on the vehicle is given by

$$\mathbf{p}' = \mathbf{p}_{cm} + \mathbf{p}_{RB} + \sum_{i=1}^{n}\boldsymbol{\phi}_i(x,y,z)\eta_i(t) \qquad\qquad 16$$

The first of Eqns. 15 governs the rigid-body translation of the body's center of mass, the second governs the rigid-body rotations of the mean-axis frame with respect to inertial, and the third governs the forced elastic deformations of the body. The inertia tensor $\mathbf{J}$ and $\overline{\Delta\mathbf{J}} = \Delta J_i + \Delta^2 J_{i,j}\eta_j$ are given in Eqns. 4 and 9. It should now be noted that the boxed terms in the first two of these three equations are identical in form to the equations of motion for a rigid vehicle. And the boxed terms in the third set of equations are the inertially decoupled equations for an elastic body undergoing forced vibrations. All the unboxed terms then represent inertial coupling between the rigid-body and elastic degrees of freedom.

Further simplifications may be justified in many practical instances. For example, if the changes in the inertia tensor, $\overline{\Delta\mathbf{J}}$, are assumed negligible and the elastic displacement $\mathbf{d}_E$ is assumed parallel to its rate of change with respect to the body frame, then $\overline{\Delta\mathbf{J}}$ and $\mathbf{h}_{i,j}$ are all zero. The latter assumption was justified in [2] by noting that the approximation is valid for beam-like and plate-like structures, as in aircraft, and hence these coupling terms would be very small compared to the aerodynamic forces. We will invoke these assumptions as well, under which J = $\mathbf{J}_0$, and the equations of motion to be used are simply the underlined boxed terms in Eqns. 15.

B. The nDOF Model – Model Structure

Considering only the longitudinal axis and assuming four control inputs, the resulting state-variable model takes the form given in Eqns. 17 below, with the first four states corresponding to the three rigid-body degrees of freedom, while the last $2n$ states corresponding to the n elastic degrees of freedom included in the model. Note that the states associated with the rigid-body degrees of freedom are identical to those in a rigid-body model. That is, in the longitudinal axes the first four states are surge velocity u_{rig}, vehicle angle of attack α_{rig}, vehicle pitch attitude θ_{rig}, and vehicle pitch rate q_{rig}, which describe the motion of the vehicle-fixed frame or mean axes. Consequently, the state vector is composed of purely rigid-body and elastic states, and note the natural partitioning of the system into rigid-body and elastic subsystems. In the rows of the A and B matrices corresponding to the elastic degrees of freedom, the terms denoted as $Z_\eta, M_\eta,$ and $\Xi_\bullet$ are dimensional aeroelastic derivatives analogous to the stability derivatives in a conventional rigid-body model.

$$\mathbf{x}^T = \begin{bmatrix} u_{rig} & \alpha_{rig} & \theta_{rig} & q_{rig} & \vdots & \eta_1 & \dot{\eta}_1 & \cdots & \eta_n & \dot{\eta}_n \end{bmatrix}$$

$$\mathbf{A} = \begin{bmatrix} X_u & X_\alpha & -g & X_q & 0 & 0 & \cdots & 0 & 0 \\ Z_u/\mathrm{U}_0 & Z_\alpha/\mathrm{U}_0 & 0 & 1+Z_q/\mathrm{U}_0 & Z_{\eta_1}/\mathrm{U}_0 & Z_{\dot{\eta}_1}/\mathrm{U}_0 & \cdots & Z_{\eta_n}/\mathrm{U}_0 & Z_{\dot{\eta}_n}/\mathrm{U}_0 \\ 0 & 0 & 0 & 1 & 0 & 0 & \cdots & 0 & 0 \\ M_u & M_\alpha & 0 & M_q & M_{\eta_1} & M_{\dot{\eta}_1} & \cdots & M_{\eta_n} & M_{\dot{\eta}_n} \\ \hdashline 0 & 0 & 0 & 0 & 0 & 1 & \cdots & 0 & 0 \\ 0 & \Xi_{1_\alpha} & 0 & \Xi_{1_q} & \Xi_{1_{\eta_1}}-\omega_1^2 & \Xi_{1_{\dot{\eta}_1}}-2\zeta_1\omega_1 & \cdots & \Xi_{1_{\eta_n}} & \Xi_{1_{\dot{\eta}_n}} \\ \vdots & \vdots & \vdots & \vdots & \vdots & \vdots & \cdots & \vdots & \vdots \\ 0 & 0 & 0 & 0 & 0 & 0 & \cdots & 0 & 1 \\ 0 & \Xi_{n_\alpha} & 0 & \Xi_{n_q} & \Xi_{n_{\eta_1}} & \Xi_{n_{\dot{\eta}_1}} & \cdots & \Xi_{n_{\eta_n}}-\omega_n^2 & \Xi_{n_{\dot{\eta}_n}}-2\zeta_n\omega_n \end{bmatrix}$$

17

$$\mathbf{A} = \begin{bmatrix} \mathbf{A}_{RR} & \vdots & \mathbf{A}_{RE} \\ \hdashline \mathbf{A}_{ER} & \vdots & \mathbf{A}_{EE} \end{bmatrix} \qquad \mathbf{B} = \begin{bmatrix} X_{\delta_1} & \cdots & X_{\delta_4} \\ Z_{\delta_1}/\mathrm{U}_0 & \cdots & Z_{\delta_4}/\mathrm{U}_0 \\ 0 & \cdots & 0 \\ M_{\delta_1} & \cdots & M_{\delta_4} \\ \hdashline 0 & \cdots & 0 \\ \Xi_{1_{\delta_1}} & \cdots & \Xi_{1_{\delta_4}} \\ 0 & \cdots & 0 \\ \Xi_{2_{\delta_1}} & \cdots & \Xi_{2_{\delta_4}} \\ 0 & \cdots & 0 \\ \Xi_{n_{\delta_4}} & \cdots & \Xi_{n_{\delta_4}} \end{bmatrix} = \begin{bmatrix} \mathbf{B}_R \\ \hdashline \mathbf{B}_E \end{bmatrix}$$

C. Model Order Reduction

Some variations on the above nDOF model involve truncating or residualizing some or all of the elastic degrees of freedom. Residualization yields a reduced-order model that retains the static-elastic effects of the residualized degrees of freedom on the aerodynamics, while truncation eliminates both the dynamics and the static-elastic aerodynamic effects of the truncated degrees of freedom.

The adjusted aerodynamic stability derivatives for a residualized model are obtained as follows (Ref. 3, Section 7.11). Assume, for example, that the number of elastic degrees of freedom included in the model, n, is three, and consider the above linearized equations of motion for the longitudinal dynamics written in the following form:

$$\dot{\mathbf{x}}_R = \mathbf{A}_{0R}\mathbf{x}_R + \mathbf{A}_{RR}\mathbf{x}_R + \begin{bmatrix} \mathbf{A}_{R\eta} & \mathbf{A}_{R\dot{\eta}} \end{bmatrix}\mathbf{x}_E + \mathbf{B}_R\mathbf{u}$$

$$\dot{\mathbf{x}}_E = \begin{bmatrix} \mathbf{0} \\ \mathbf{A}_{ER} \end{bmatrix}\mathbf{x}_R + \begin{bmatrix} \mathbf{0} & \mathbf{I} \\ \mathbf{A}_{0\eta} & \mathbf{A}_{0\dot{\eta}} \end{bmatrix}\mathbf{x}_E + \begin{bmatrix} \mathbf{0} & \mathbf{0} \\ \mathbf{A}_{E\eta} & \mathbf{A}_{E\dot{\eta}} \end{bmatrix}\mathbf{x}_E + \mathbf{B}_E\mathbf{u}$$

18

where the rigid-body and elastic states, control inputs, etc. are given as

$$\mathbf{x}_R = \begin{Bmatrix} u_{rig} \\ \alpha_{rig} \\ \theta_{rig} \\ q_{rig} \end{Bmatrix}, \quad \mathbf{x}_E = \begin{Bmatrix} \boldsymbol{\eta} \\ \dot{\boldsymbol{\eta}} \end{Bmatrix} = \begin{Bmatrix} \eta_1 \\ \eta_2 \\ \eta_3 \\ \dot{\eta}_1 \\ \dot{\eta}_2 \\ \dot{\eta}_3 \end{Bmatrix}, \quad \mathbf{u} = \begin{Bmatrix} \delta_1 \\ \delta_2 \\ \delta_3 \\ \delta_4 \end{Bmatrix}, \quad \mathbf{A}_{0R} = \begin{bmatrix} 0 & 0 & -g & 0 \\ 0 & 0 & 0 & 1 \\ 0 & 0 & 0 & 1 \\ 0 & 0 & 0 & 0 \end{bmatrix} \qquad 19$$

$$\mathbf{A}_{0\eta} = \begin{bmatrix} -\omega_1^2 & 0 & 0 \\ 0 & -\omega_2^2 & 0 \\ 0 & 0 & -\omega_3^2 \end{bmatrix}, \quad \mathbf{A}_{0\dot{\eta}} = \begin{bmatrix} -2\zeta_1\omega_1 & 0 & 0 \\ 0 & -2\zeta_2\omega_2 & 0 \\ 0 & 0 & -2\zeta_3\omega_3 \end{bmatrix}$$

The elements of the remaining matrices are dimensional stability derivatives such as M_α in the aerodynamic model for the forces, moments, and generalized forces. These matrices are discussed further in Sec.V.

Setting the elastic-state rates to zero, for example, and solving for the static-elastic displacements we have

$$\boldsymbol{\eta}_o = -\left(\mathbf{A}_{0\eta} + \mathbf{A}_{E\eta}\right)^{-1}\left(\mathbf{A}_{ER}\mathbf{x}_R + \mathbf{B}_E\mathbf{u}\right) \qquad 20$$

And after substituting this constraint back into the EOM's we have the residualized reduced-order model (ROM) for the rigid-body degrees of freedom only given by

$$\dot{\mathbf{x}}_R = \mathbf{A}_{0R}\mathbf{x}_R + \left(\mathbf{A}_{RR} - \mathbf{A}_{R\eta}\left(\mathbf{A}_{0\eta} + \mathbf{A}_{E\eta}\right)^{-1}\mathbf{A}_{ER}\right)\mathbf{x}_R + \left(\mathbf{B}_R - \mathbf{A}_{R\eta}\left(\mathbf{A}_{0\eta} + \mathbf{A}_{E\eta}\right)^{-1}\mathbf{B}_E\right)\mathbf{u} \qquad 21$$

$$= \mathbf{A}_{ROM}\mathbf{x}_R + \mathbf{B}_{ROM}\mathbf{u}$$

The dimensional aerodynamic derivatives adjusted for static-elastic deflections are then the elements of

$$\left(\mathbf{A}_{RR} - \mathbf{A}_{R\eta}\left(\mathbf{A}_{0\eta} + \mathbf{A}_{E\eta}\right)^{-1}\mathbf{A}_{ER}\right) \text{ and } \left(\mathbf{B}_R - \mathbf{A}_{R\eta}\left(\mathbf{A}_{0\eta} + \mathbf{A}_{E\eta}\right)^{-1}\mathbf{B}_E\right) \qquad 22$$

III. The Study Vehicle

The vehicle of interest, depicted in Figs. 2 and 3, was designed and constructed at the University of Minnesota (UMN) [11], and is similar to Lockheed Martin's Free-Flight Aeroelastic Demonstrator vehicle [1,12]. Our vehicle is a 14.7-pound unmanned, flying-wing aircraft with a 10 ft wingspan. The vehicle is designed to exhibit two symmetric flutter conditions in the longitudinal axis, involving the first two symmetric aeroelastic modes. Flutter is also exhibited in the lateral-directional axes, but the focus here will be on the longitudinal dynamics.

The vehicle is a low-speed swept-back flying wing with winglets on the wing tips for directional stability and an electric motor driving a pusher propeller (not shown in the figure) mounted at the top rear of the rigid center body. The entire trailing edge of the wing consists of eight control surfaces, including body flaps (surfaces L1 and R1). The vehicle's mass properties and the planform characteristics are summarized in Tables A1 and A2 in Sec. X, Appendix A. Note that this is a fairly small, lightweight, unmanned vehicle.

The wing is mainly composed of a solid spar and the wing foam, as depicted in Fig. 4. The spar was fabricated from a foam core with composite laminated reinforcements surrounding the core. The foam core material is extruded polystyrene (XPS). The material for the reinforcement is carbon fiber fabric in the form of a plane weave with 3K tow. The composite matrix is a laminating epoxy. The wing foam that contributes to both the outer model line (OML) and the wing mass is EPS 1.5# with a dry fabric made of E-glass fabric plane weave.
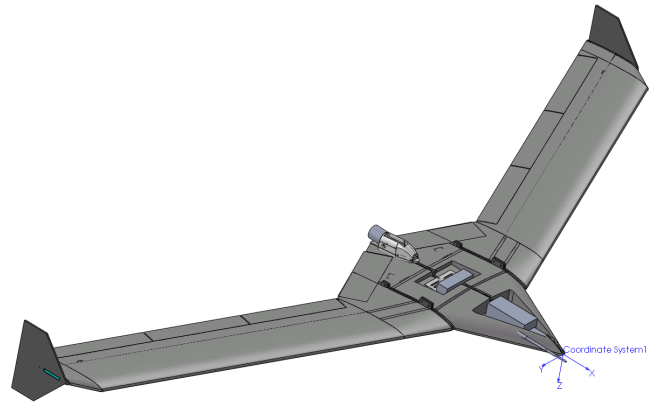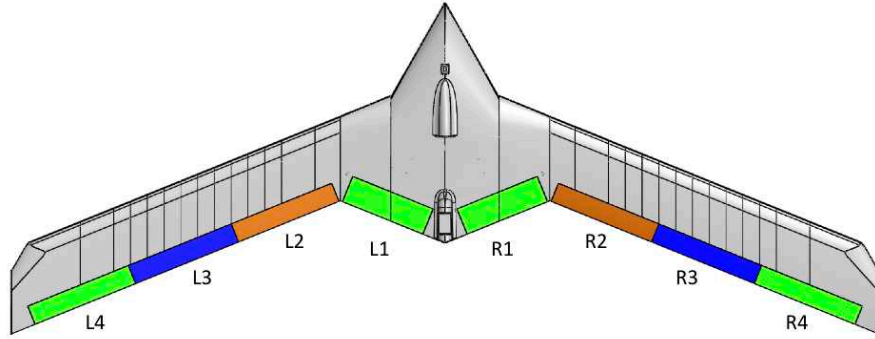

Figure 2, Vehicle Configuration

American Institute of Aeronautics and Astronautics

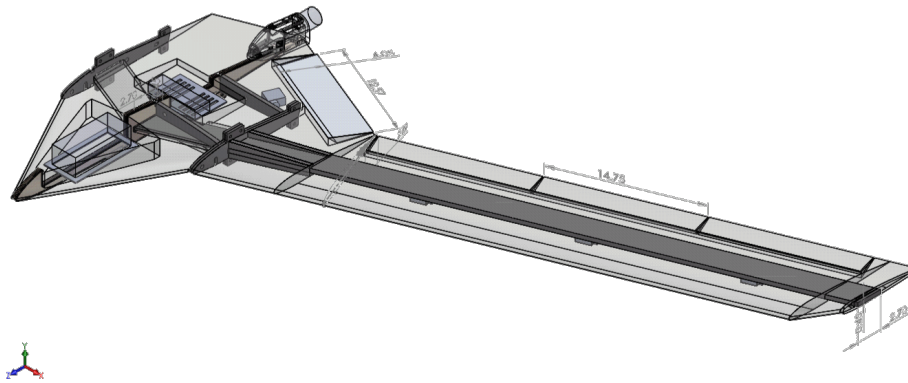**Figure 3, Planform Schematic**

Figure 4, Internal View, Left Wing and Centerbody

IV. Structural Dynamics - Finite-Element Model (FEM)

A finite-element model FEM was developed in MSC/NASTRAN [2] and used to characterize the vehicle's structural-vibration properties. The nodal geometry and structural coordinate frame used in the FEM are shown in Fig. 5. The model is based on beam and rod elements, and the use of such elements reduces the order of the stiffness and mass matrices for an efficient and accurate flutter analysis.
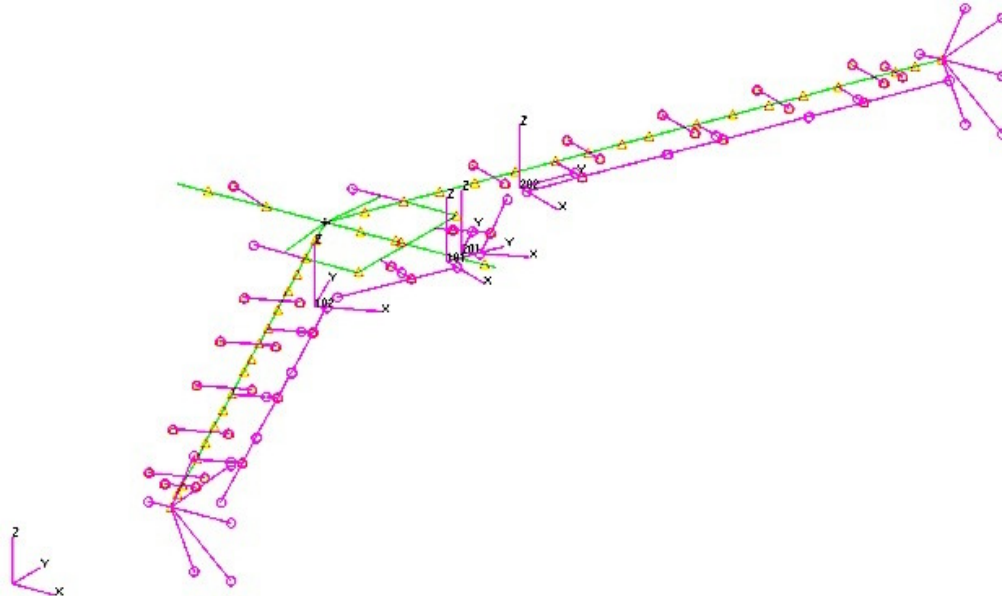
Figure 5, Finite-Element Coordinate Frame and Node Schematic

The centerbody of the vehicle was modeled as a rod with several point masses. The flight computer, propulsion battery, engine motor, body flap, servos and accelerometers are all modeled as point masses, and the moments of inertia of the flight computer and the propulsion battery are included. The wires, foam, and cover fabric for the centerbody were modeled as point masses located at the spar beam element nodes. The hinge bolt for the connection between the body flap and the centerbody was modeled as a spring element with a large spring stiffness.

The wing is modeled as a beam and the elastic axis of the wing is assumed to lie along the mid-chord of the solid spar. Variable stiffness EI, GJ and GA along the wing span were selected to match static and vibration ground tests, and additional lumped masses located at the outer wing beam element nodes are included to match the mass properties.

The stiffening members through the centerbody, such as the front and rear spars, are modeled as beams, as are the wing attachments connecting the wing to the centerbody. The control surfaces in the wing are modeled as point masses. Many massless nodes connected to the main wing through rigid connections are also included in the FEM to spline the structural deformation to the aero mesh for flutter analysis.

The mass distribution for both the wing and the centerbody are updated based on the test data, and the mass properties for the updated FEM agree well with the test data obtained for the complete vehicle, as shown in Table A1 in Sec. X, Appendix A.

The free-vibration-modal results from the FEM are summarized in Table 1 for the first three symmetric modes. A ground-vibration test was conducted, but the data were considered unreliable and not used in this analysis. As a result, modal damping ratios of 2 percent were assumed. Note that these vibration frequencies are slightly higher than those for the vehicle considered in [1], as a result of stiffer wings.

Table 1, Structural Vibration Characteristics

Data and Source	1st Sym. Mode	2nd Sym. Mode	3rd Sym. Mode
Mode Identification	"Sym 1st Bending"	"Sym 1st Torsion"	"Sym 2nd Bending"
Frequency, NASTRAN FEM	6.07 Hz	12.15 Hz	19.47 Hz
Damping Ratio (assumed)	2.0%	2.0%	2.0%
Gen. Mass, NASTRAN FEM	1 sl-ft/in	1 sl-ft/in	1 sl-ft/in

The mode shapes for the first three symmetric modes are shown in Figs. 6-8, respectively. The first mode exhibits both bending and wing torsion, but will be referred to as the symmetric-first-bending mode; The second mode exhibits primarily wing torsion, and will be referred to as the symmetric first torsion mode; and the third mode will be referred to as the symmetric second bending mode, although some torsion is also exhibited.

In another view of the mode shapes, the transverse and torsional displacements along the elastic axis are shown for the first two of these free-vibration modes in Figs. 9-10. These data are used to calculate the aeroelastic stability derivatives. From the FEM coordinate definitions, the plunge-translational displacement (Z vehicle positive up) and wing torsional (pitch θ positive leading-edge up) displacement along the wing elastic axis are both indicated. Consequently, it is clear from Figs. 6 and 9 that the first symmetric mode exhibits simultaneous (tips-down) bending and (leading-edge-down) torsional displacements. The second symmetric mode shape in Figs. 7 and 10 exhibits primarily torsional displacement. Chord-wise bending is essentially non-existent in all three of these symmetric modes.
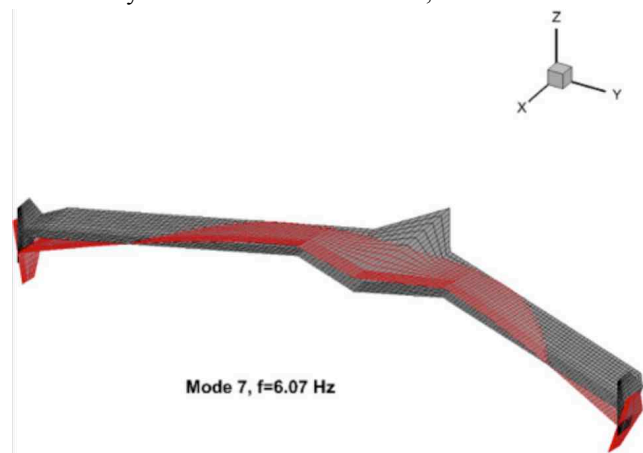

Mode 7, f=6.07 Hz

Figure 6, Mode Shape – First Symmetric Free-Vibration Mode
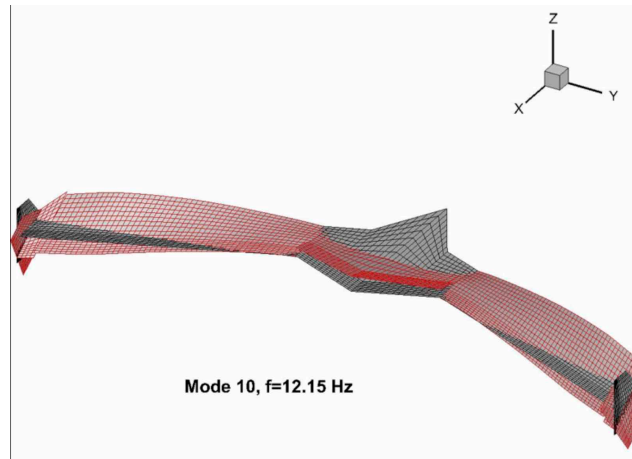
Figure 7, Mode Shape – Second Symmetric Free-Vibration Mode

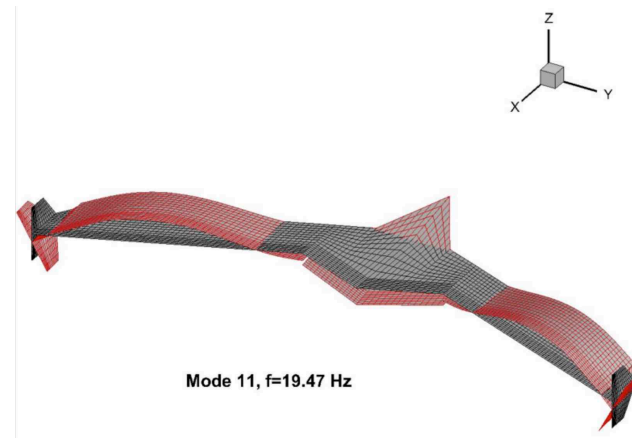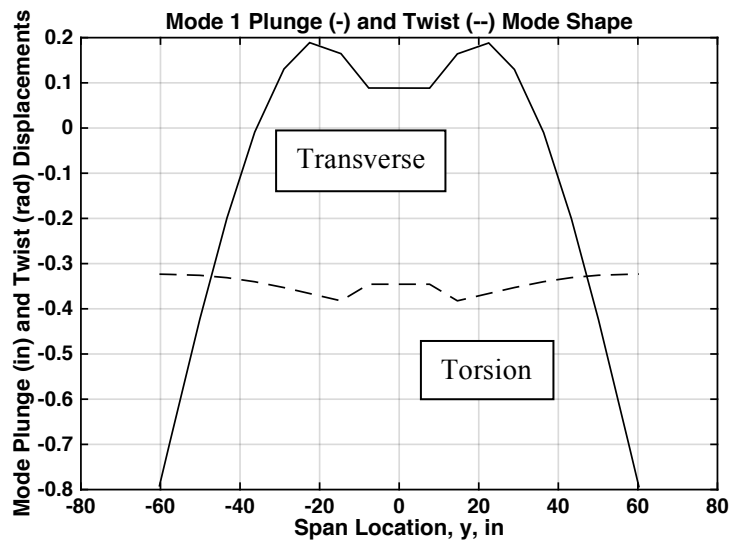**Figure 8, Mode Shape – Third Symmetric Free-Vibration Mode**

Figure 9, Mode Shape Along Elastic Axis, First Symmetric Mode

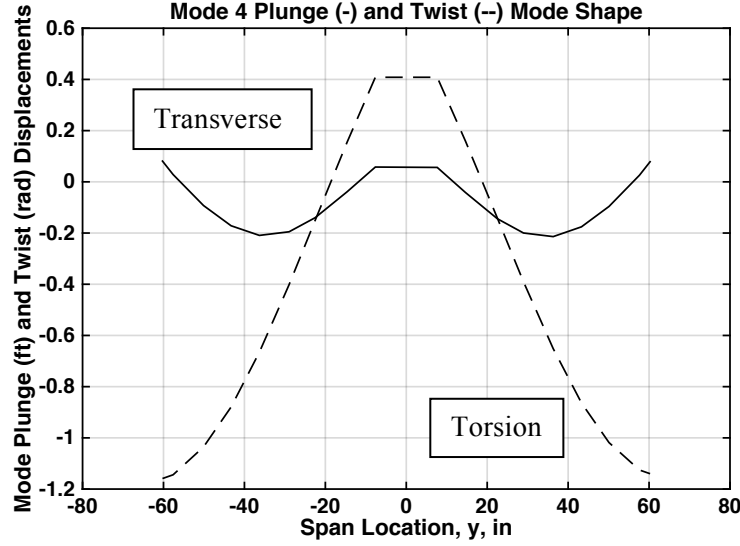American Institute of Aeronautics and Astronautics

Figure 10, Mode Shape Along Elastic Axis, Second Symmetric Mode

V. Aerodynamic Modeling

The aerodynamic forces and moments acting on the vehicle arise from both rigid-body motion and elastic deformation. Or, as discussed in Ref. 3, Chapters 6 and 7, and consistent with small disturbance theory, the vector of generalized aerodynamic forces and moments $\mathbf{F}$, may be expressed as

$$\mathbf{F} = \mathbf{A}_R \mathbf{x}_R + \mathbf{A}_E \mathbf{x}_E + \mathbf{B}_C \mathbf{u} \qquad 23$$

where
- $\mathbf{x}_R$ = state vector representing the rigid-body DOF's (u_{rig}, w_{rig} or α_{rig}, θ_{rig}, q_{rig})
- $\mathbf{x}_E$ = state vector consisting of elastic modal coordinates (η_i, $\dot{\eta}_i$ the free-vibration modal coordinates)
- $\mathbf{u}$ = vector of control-surface displacements
- $\mathbf{A}_R$, $\mathbf{A}_E$, $\mathbf{B}_C$ = matrices of dimensional stability derivatives – both rigid-body and aeroelastic

By appropriately partitioning the vector $\mathbf{F}$ and the matrices above, let's define

$$\mathbf{F} = \begin{bmatrix} \mathbf{F}_R \\ \mathbf{F}_E \end{bmatrix}, \qquad \mathbf{A}_R \triangleq \begin{bmatrix} \mathbf{A}_{RR} \\ \mathbf{A}_{RE} \end{bmatrix}, \qquad \mathbf{A}_E \triangleq \begin{bmatrix} \mathbf{A}_{ER} \\ \mathbf{A}_{EE} \end{bmatrix}, \qquad \mathbf{B}_C \triangleq \begin{bmatrix} \mathbf{B}_R \\ \mathbf{B}_E \end{bmatrix} \qquad 24$$

Now note that the elements of the matrices $\mathbf{A}_{RR}$ and $\mathbf{B}_R$ are functions of the rigid-body stability derivatives, and are included in a flight-dynamics model of the rigid vehicle in its <u>undeformed shape</u>, since $\mathbf{F}_R$ (without the elastic contributions) would be incorporated in that model. The remaining dimensional derivatives in the matrices $\mathbf{A}_{RE}$, $\mathbf{A}_{ER}$, $\mathbf{A}_{EE}$, and $\mathbf{B}_E$ are to be discussed below.

The rigid-body aerodynamic characteristics of the undeformed vehicle were estimated using a public-domain, MATLAB®-based, vortex-lattice code [13]. The aerodynamic grid for the vehicle is shown in Fig. 11, and the estimated stability derivatives are presented in Table B1 in Sec. X, Appendix B for the rigid-vehicle in its undeformed shape. Note that the $\dot{\alpha}$ derivatives, primarily associated with lag of downwash on a trailing lifting surface, are typically negligible on a flying wing. Based on these data note that the rigid vehicle is statically stable, with a static margin of

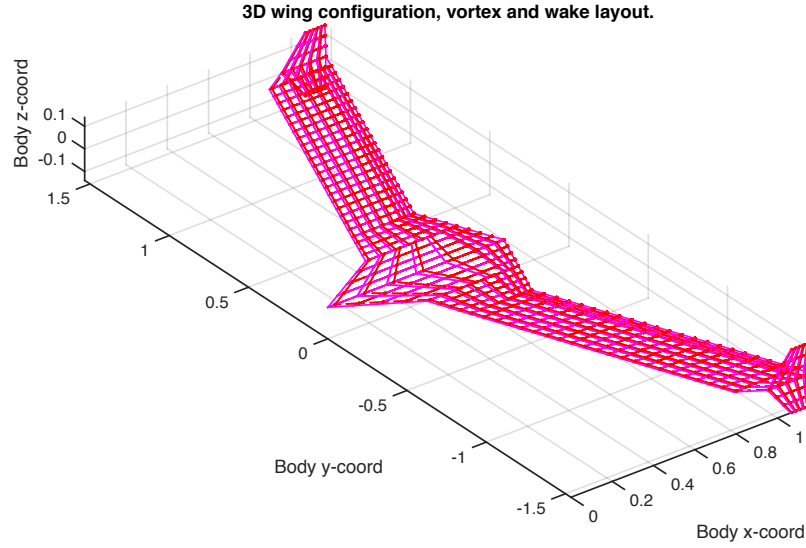$$SM = \frac{-C_{M_\alpha}}{C_{L_\alpha}} = \frac{0.154}{4.592} = 3.4\% \qquad 25$$

3D wing configuration, vortex and wake layout.

Figure 11, Vortex-Lattice Grid (dimensions shown in meters)

Considering only the longitudinal forces and pitching moment F_X, F_Z, and M, and the generalized forces acting on the *n* symmetric vibration-modal coordinates, the four remaining matrices of interest in Eqn. 24 above may be written as

$$\mathbf{A}_{RE} = q_\infty S\bar{c} \begin{bmatrix} C_{Q_{1u}} & C_{Q_{1w}} & 0 & C_{Q_{1q}} \\ \vdots & \vdots & \vdots & \vdots \\ C_{Q_{nu}} & C_{Q_{nw}} & 0 & C_{Q_{nq}} \end{bmatrix}, \quad \mathbf{A}_{ER} = diag\left(q_\infty S, q_\infty S, q_\infty S\bar{c}\right) \begin{bmatrix} C_{X_{\eta_1}} & C_{X_{\dot{\eta}_1}} & \cdots & C_{X_{\eta_n}} & C_{X_{\dot{\eta}_n}} \\ C_{Z_{\eta_1}} & C_{Z_{\dot{\eta}_1}} & \cdots & C_{Z_{\eta_n}} & C_{Z_{\dot{\eta}_n}} \\ C_{M_{\eta_1}} & C_{M_{\dot{\eta}_1}} & \cdots & C_{M_{\eta_n}} & C_{M_{\dot{\eta}_n}} \end{bmatrix}$$

$$\mathbf{A}_{EE} = q_\infty S\bar{c} \begin{bmatrix} C_{Q_{1\eta_1}} & C_{Q_{1\dot{\eta}_1}} & \cdots & C_{Q_{1\eta_n}} & C_{Q_{1\dot{\eta}_n}} \\ \vdots & \vdots & \vdots & \vdots & \vdots \\ C_{Q_{n\eta_1}} & C_{Q_{n\dot{\eta}_1}} & \cdots & C_{Q_{n\eta_n}} & C_{Q_{n\dot{\eta}_n}} \end{bmatrix}, \quad \mathbf{B}_E = q_\infty S\bar{c} \begin{bmatrix} C_{Q_{1u_1}} & \cdots & C_{Q_{1u_m}} \\ \vdots & \vdots & \vdots \\ C_{Q_{nu_1}} & \cdots & C_{Q_{nu_m}} \end{bmatrix}$$

26

As discussed in Ref. 3, Chapter 7, various methods exist to estimate the aeroelastic coefficients appearing in the above four matrices. Unsteady-aerodynamic effects will be assumed negligible here. If unsteady affects are deemed necessary to more accurately capture the flutter speeds, they may be added at a later time.

Using integral expressions based on virtual-work concepts given in Ref. 3, Chapter 7, plus those given in [1], the aeroelastic coefficients for our vehicle are given in Table B2 in Section X, Appendix B. These integral expressions, all evaluated in MATLAB®, are functions of the wing geometry, the free-vibration mode shapes, and the span-wise distribution of the lift effectiveness, $c_{l_\alpha}(y)$, shown in Fig. 12. This distribution was also obtained using the vortex-lattice aerodynamics code cited previously. The effect of elastic deformation on the vehicle drag is assumed negligible. Several of the coefficients are inversely proportion to the flight velocity, so for these coefficients the values listed in the table is the coefficient's value multiplied by flight velocity. Finally, the four control deflections $\delta_1 - \delta_4$ correspond to symmetric deflections of control surfaces one through four along the wings, respectively, as shown in Fig. 3.
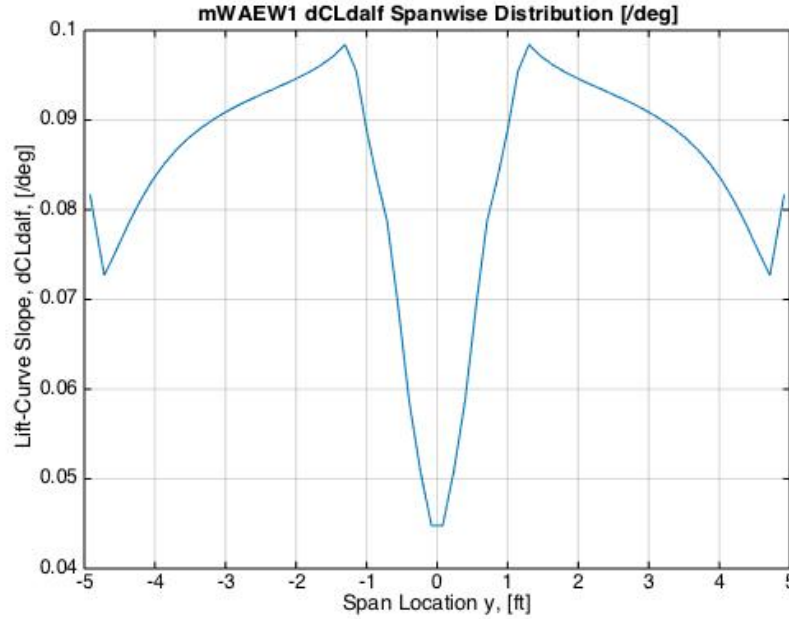
Figure, 12, Spanwise Distribution of Lift Effectiveness

VI. Longitudinal Flight Dynamics

A. Rigid-Body Longitudinal Dynamics

We first consider the longitudinal dynamics of the rigid vehicle in its undeformed shape. For a level-flight condition of 1000 ft altitude and a velocity of 50.5 kt, the transfer functions for the pitch-attitude and plunge-acceleration (at the *cg*) responses from symmetric deflections of surfaces L3 and R3 shown in Fig. 3 (defined here as elevator deflections δ_3) are

$$\frac{\theta_{cg}(s)}{-\delta_3(s)} = \frac{65.2\,[0.014][10.4]}{[-0.02,0.38][0.80,10.0]} \quad \text{deg/deg}$$

27

$$\frac{n_{Z-cg}(s)}{-\delta_3(s)} = \frac{0.943\,[0.32][-0.34][25.4][-31.4]}{[-0.02,0.38][0.80,10.0]} \quad \text{ft/s}^2/\text{deg}$$

(Here a shorthand notation in used. Two terms in square brackets denote the damping and frequency of a quadratic polynomial, and a single term in brackets denotes the negative of the root of a first-order polynomial.) The complex phugoid mode is slightly unstable with a natural frequency of 0.38 rad/sec, while the short period is stable and well damped with a natural frequency of 10.0 rad/sec. Also, the attitude numerator roots are $1/T_{\theta_1} = 0.014$ /sec and $1/T_{\theta_2} = 10.4$ /sec. The pitch-rate step response to a negative one-degree elevator deflection is shown in Fig. 13

The eigenvector, or mode shape, for the short-period mode is a traditional short-period mode shape (See Ref. 3 Chapter 10.). That is, the mode is dominated by the pitch-rate response, with angle of attack and pitch attitude making moderate contributions to the modal response. These latter
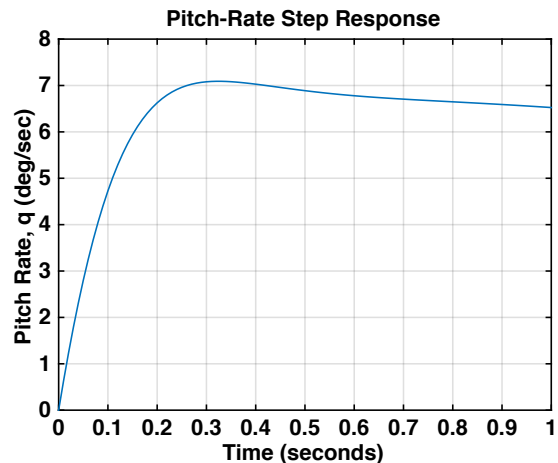

Figure 13, Pitch-Rate Step Response-Rigid Vehicle

13

American Institute of Aeronautics and Astronautics

two responses, furthermore, lag the pitch rate in phase. The contribution of surge velocity u to the short-period response is essentially zero. Note that rather conventional aircraft attitude dynamics are exhibited.

B. Flexible-Vehicle Longitudinal Dynamics

Now considering the flexible vehicle including the three elastic degrees of freedom, the transfer functions for the pitch attitude and plunge acceleration (measured at the vehicle's *cg* on the center-body centerline) from elevator (δ_3) are given in Eqns. 28. The flight condition is 1000 ft altitude and 50.5 kt velocity, which is below the critical flutter speed. These two dynamic responses include the effects of dynamic elastic deformations at that point on the structure corresponding to the *cg* location of the undeformed vehicle. When comparing these transfer functions with those for the rigid vehicle given in Eqns. 27, note that the modal frequency and damping ratio of the second mode (originally the short-period mode) have been modified. Also, the zeros in both transfer functions, corresponding to those in Eqns. 27, have been affected. In particular, $1/T_{\theta_1} = 0.017$ /sec and $1/T_{\theta_2} = 10.7$ /sec. Since $1/T_{\theta_2}$ is roughly proportional to the lift effectiveness Z_α, we see that the lift effectiveness has been increased due to the wing twisting. This will be discussed further later in this section. The presence of the aeroelastic modes is indicated by the three sets of higher-frequency dipoles (pole-zero pairs) in each of these transfer functions.

$$\frac{\theta_{cg}(s)}{-\delta_3(s)} = \frac{36.2\ [0.017][10.7][0.26,41.7][-0.08,55.3][0.03,201.7]}{[-0.02,0.43][0.70,14.0][0.07,33.4][0.03,71.1][0.04,122.0]}\ \text{deg/deg}$$

$$\frac{n_{Z-cg}(s)}{-\delta_3(s)} = \frac{0.942\ [0][-0.01][24.13][-24.18][0.13,38.9][0.02,68.2][0.01,179.7]}{[-0.02,0.43][0.70,14.0][0.07,33.4][0.03,71.1][0.04,122.0]}\ \text{ft/sec}^2\text{/deg}$$

28

The complex, slightly unstable phugoid mode is noted, while the second mode, with a natural frequency of around 14 rad/sec, corresponds to the short-period mode of the rigid vehicle. However, it is no longer a classical short-period mode. This mode's eigenvector (or mode shape), after a state transformation that non-dimensionalizes the surge velocity u (= u/U_0) and converts the elastic states to elastic pitch deformation (twist) measured at the vehicle centerline θ_{E1}, θ_{E2}, and θ_{E3}, is depicted in Fig. 14. Note that as in [1], and unlike a conventional short-period mode shape, the second largest contributor to this modal response is the elastic-pitch-rate displacement associated with the first aeroelastic degree of freedom $\dot{\theta}_{E1}$. For the rigid vehicle this component is of course absent in the short-period modal response, and the second largest contributors are rigid-body angle of attack α_{rig} and pitch attitude θ_{rig}. So as in a true short-period mode, there is virtually no surge velocity u_{rig} present in the mode shape, the mode is dominated by the rigid-body pitch-rate response of the vehicle q_{rig}, and the phase relationships between pitch rate, pitch attitude, and angle of attack are as in the conventional short-period mode. But this mode is a coupled rigid-body and elastic mode.
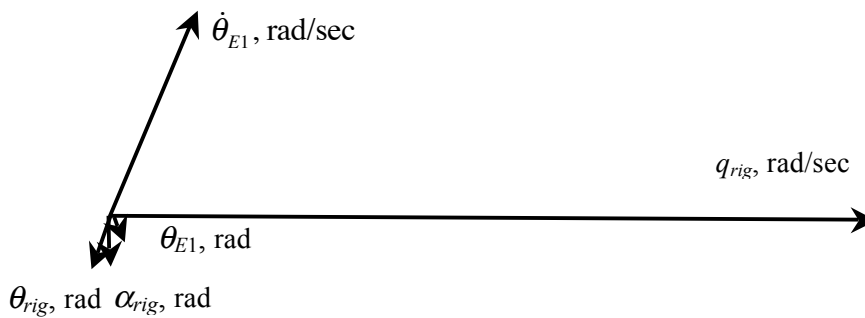

Figure 14, "Elastic Short-Period" Mode Eigenvector (Mode Shape)

The next-highest-frequency mode reflected in the transfer functions is the lightly damped first aeroelastic mode (AE Mode 1), with an undamped natural frequency of approximately 33 rad/sec. This mode is also a coupled rigid-body/elastic mode, but is dominated by the elastic-pitch-rate deformation at the vehicle's center body associated with the first elastic (bending-torsion) degree of freedom, $\dot{\theta}_{E1}$.

The next largest contributor to this modal response is the rigid-body pitch rate (or the pitch rate of the mean axis of the vehicle) q_{rig}. And the next largest contributor after that is elastic pitch rate of the center body associated with the second elastic degree of freedom $\dot{\theta}_{E2}$. There are also small contributions from the rigid-body angle of attack and pitch attitude, and there is again virtually no surge velocity u_{rig} present in this modal response. So as with the elastic-short-period mode in Fig. 14, this first aeroelastic mode exhibits rigid-elastic coupling, leading to a body-freedom-flutter condition at higher flight velocity.

The Bode plot of the pitch rate from (negative) elevator deflection, measured at the point on the structure corresponding to the *cg* location of the undeformed vehicle are shown by the solid lines in Fig. 15. The dashed lines are the frequency response for the rigid, undeformed vehicle. The flight velocity in this case is 50.5 kts, or 85.3 fps. The lightly damped unstable phugoid mode is evident in both responses. In the flexible response, the magnitude and phase contributions from the well-damped short-period-like mode near 14 rad/sec merges with those from the first aeroelastic mode near 33 rad/sec, leading to a significant phase difference compared to the rigid-body phase near the short-period frequency. The two dipoles associated with the lightly-damped aeroelastic modes near 71 and 122 rad/sec are also evident.

At the same flight condition, the step responses for the pitch rate and (negative) plunge acceleration at the cg location of the undeformed vehicle, as well as the vehicle (mean-axis) angle of attack are shown in Figs. 16a and b. The input is negative one degree of elevator deflection, δ_3. The aeroelastic dynamics are clearly evident in these quick responses, and the pitch-rate response differs considerably from that for the rigid vehicle shown in Fig. 13.

As a final topic, we will discuss a reduced-order model of the elastic vehicle,

Figure 15, Bode Plot – Pitch Rate (q_{cg}) From Negative Elevator (deg/sec/deg)
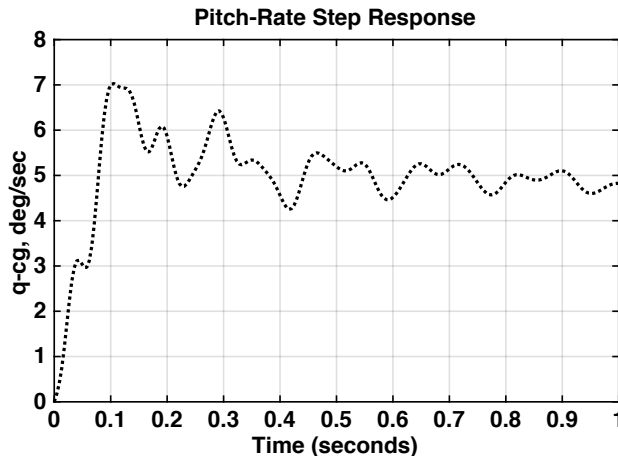
Figure 16a, Pitch-Rate (cg) Elevator Step Response

obtained by residualizing all three elastic degrees of freedom, yielding a model for the dynamics of the rigid-body degrees of freedom only, but including the effects of <u>static</u> displacements of the elastic degrees of freedom. This model represents the "rigid-body" dynamics of the vehicle in its in-flight shape under load, as opposed to the rigid-body model that reflects the dynamics of the vehicle in its undeformed. The resulting adjusted non-dimensional aerodynamic coefficients for our vehicle are listed in Table B3 in Section X, Appendix B.

When one compares the aero derivatives in Table B3 with those for the rigid vehicle in Table B1, several large differences may be noted. And these differences of course, are due to the static deformation of the structure.
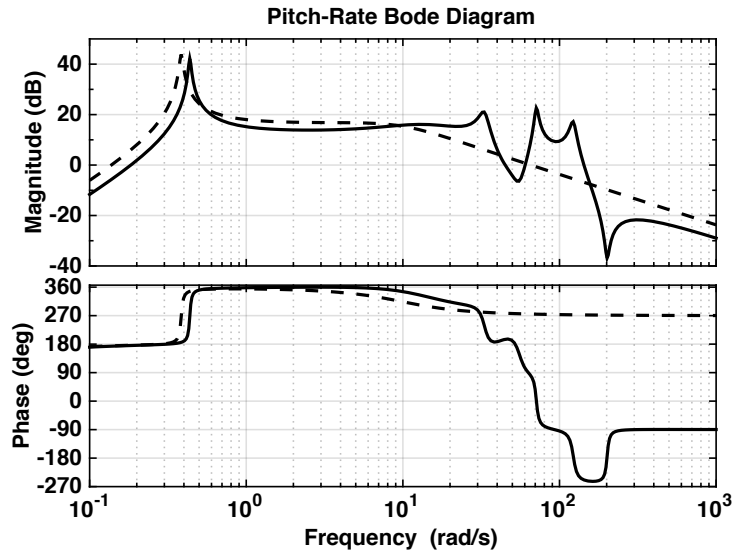
Consider, for example, the effect of angle of attack on the lift and pitching moment, or C_{L_α} and C_{M_α}. As the angle of attack increases, the bending moment on the wing increases, which tends to bend the flexible wing. But from the mode shape of the first symmetric mode in Figs. 6 and 9, as the wing bends up it also twists leading-edge up. And this further increases the angle of attack of the wing. The effect is to drastically increase the effect of vehicle angle of attack on lift and pitching moment. Similar analyses help explain the changes in effectiveness of the control surfaces, for example. Control-surface deflections not only increase the wing lift due to changes in camber, but also twist the wing in the direction opposite to the surface deflection. Fortunately, however, no static control

Figure 16b, Mean-Axis Angle-of-Attack and Plunge-Acceleration (cg) Step Responses

reversals are indicated in the data. That is, all positive control deflections increase vehicle lift and induce a negative pitching moment. But it should be clear from these results that this vehicle is very flexible with quick attitude response. And the effects of flexibility make the pitch response even faster.

The pitch-rate and plunge acceleration transfer functions from this residualized reduced-order model at 50.5 fps, corresponding to Eqns. 27 and 28, are

$$\frac{\theta_{cg}(s)}{-\delta_3(s)} = \frac{75.4\,[0.013][12.4]}{[-0.02,0.44][0.73,14.2]} \quad \text{deg/deg}$$

$$\frac{n_{Z-cg}(s)}{-\delta_3(s)} = \frac{2.22\,[0][-0.01][24.7][-25.4]}{[-0.02,0.44][0.73,14.2]} \quad \text{ft/sec}^2/\text{deg}$$

29

Clearly these transfer functions differ significantly from those given in Eqns. 27 for the rigid vehicle. The short-period damping and frequency differ due to the changes in effective C_{m_α} and C_{m_q}, and $1/T_{\theta 2}$ is increased due to the increase in C_{L_α}.

A final comparison between the three models we've developed is given in Fig. 17, which shows the pitch-rate step responses from negative 1-deg elevator deflection plotted in deg/sec/deg. The "Rigid Model" response corresponds to Eqns. 27, the "Static-Elastic Corrected" response is the response from the residualized reduced-order model being discussed here (Eqns. 29), and the "Full-Order" response is from the full-order model, or Eqns. 28. These responses differ significantly, indicating the degree of flexibility in this vehicle. Comparing the first two responses reveals the effects of the static-elastic deflections of the structure, while comparing the last two responses reveals the effects of the dynamic response of the structure.
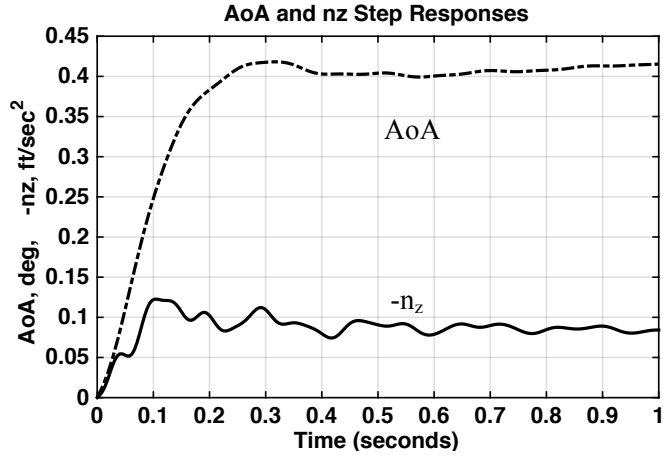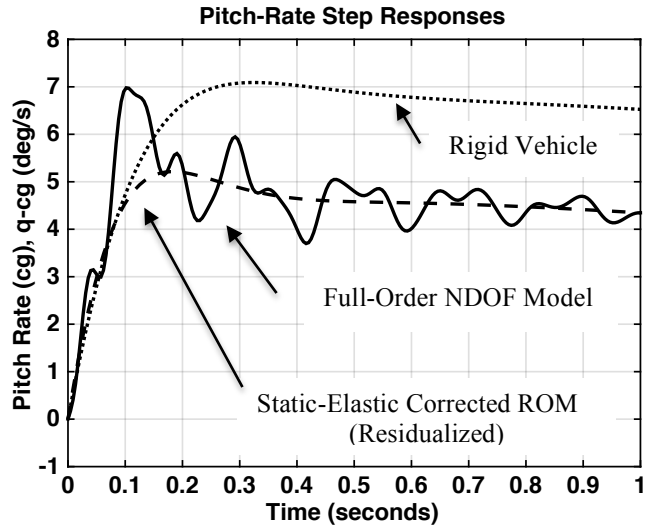

Figure 17, Pitch-Rate Step Response From δ_3 (deg/s/deg)

Transient responses from the FD model were also compared to those from flight test, and the model was further updated with adjusted aerodynamic coefficients based on parameter-identification [14]. Some results from that investigation are shown in Fig. 18, in which the transient responses for wing-tip acceleration plotted in meters/sec^2 measured in flight are compared to those from the FD model both before and after aero-coefficient updating. The inputs are three separate elevator control reversals using a 3-2-1-1 pattern. These two model-based responses are seen to agree quite well to those measured, even before parameter updating. Thus providing additional validation of the models presented in this paper.
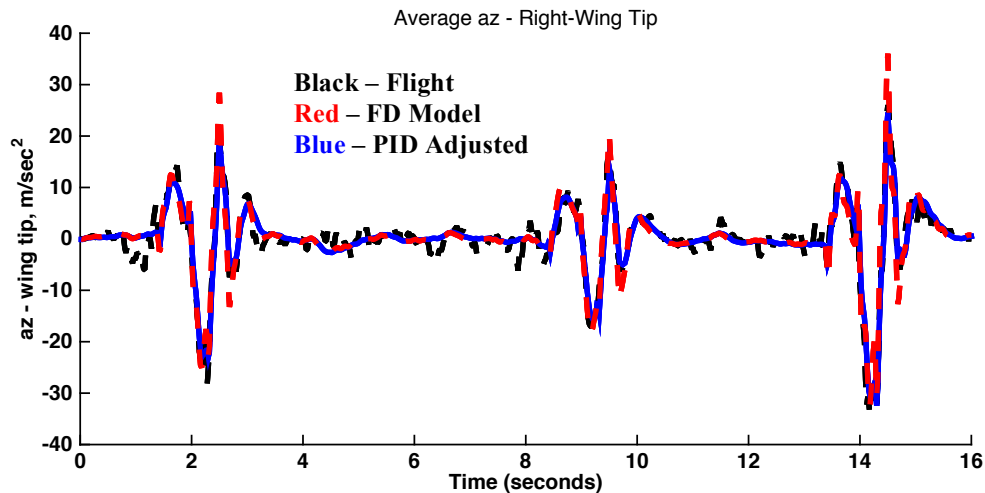

Figure 18, Comparison of Wing-Tip Transient Responses With Flight-Test Data

VII. Flutter Analysis

A. Flutter Analysis via MSC/NASTRAN

A flutter analysis was performed in NASTRAN, considering both all six rigid-body and several symmetric and anti-symmetric elastic degrees of freedom. The doublet lattice 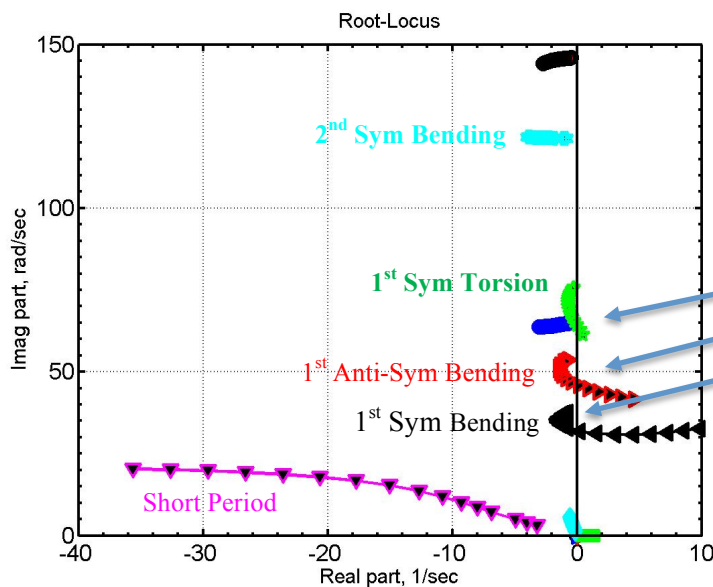method was used for unsteady aerodynamic modeling, and the aero mesh is similar to that shown in Fig. 11. The p-k method [15] was used to obtain the flutter solution, and the dynamic-pressure root-locus is shown in Fig. 19. The relevant branches in the figure are labeled according to their genesis rigid-body or free-vibration modes. Three flutter conditions are noted, two in the longitudinal axis involving symmetric modes, including body-freedom flutter (BFF), and one in the lateral-directional axis involving anti-symmetric modes. These three conditions are summarized in Table 2. We will discuss the two symmetric flutter conditions more below in the next section, but body-freedom flutter involves the interaction between the rigid-body and first symmetric aeroelastic mode.

Figure 19, Dynamic-Pressure Root Locus Obtained From NASTRAN

Table 2, Summary of The Three Flutter Conditions Obtained from NASTRAN

Flutter Mode	Flutter Speed (Knots)	Flutter Frequency (Hz)
BFF (symmetric)	63.65	5.10
Flutter Mode 2 (anti-symmetric)	73.19	7.36
Flutter Mode 3 (symmetric)	89.46	10.23

B. Flutter Analysis via the Flight-Dynamics (FD) Model

Now consider Fig. 20, showing the dynamic-pressure root locus showing the system's longitudinal, symmetric eigenvalues of the FD model, discussed in the previous sections, as a function of dynamic pressure. The eigenvalue locations are shown for seven flight velocities between 30 and 70 kt. The system modes (locus branches) are again labeled according to their <u>modal genesis</u>, or the mode branches are identified according to their genesis mode of pure rigid-body mode or pure free-vibration mode. But to be clear, all the modes involve coupling through the aerodynamics, and hence are not pure short period, pure bending-torsion vibration, etc. The similarity between Fig. 20 and the longitudinal results in Fig. 19 from the NASTRAN model is obvious.

Now consider the branch labeled "Short Period." As the flight velocity, or dynamic pressure, increases, the roots move farther into the left-half plane. The next branch labeled "1st Sym. Bending" begins at the pole from the first symmetric-bending vibration mode, almost on the imaginary axis at 34.2 rad/sec (the free-vibration frequency), and initially moves further into the left-half plane at lower flight velocities. As flight velocity continues to increase, this branch loops back around to the right and eventually crosses the imaginary axis. This axis crossing corresponds to the flutter condition known as body-freedom flutter (BFF), and for this model BFF occurs at a flight velocity of approximately 63 kt and with a flutter frequency of 30 rad/sec (4.8 Hz). Body-freedom flutter is a unique aeroelastic phenomenon that involves interactions between the rigid-body and elastic DOFs, or the "short-period" and the "first-bending" modes here. If the rigid-body degrees of freedom are truncated, the BFF condition is absent.

Next, with regard to the branch labeled "1st Sym. Torsion," it begins at the pole arising from the second symmetric vibration mode, almost on the imaginary axis at 117.8 rad/sec, and also begins moving into the left-half plane. As flight velocity continues to increase, it also curves back to the right and will ultimately cross the imaginary axis, indicating another flutter mode
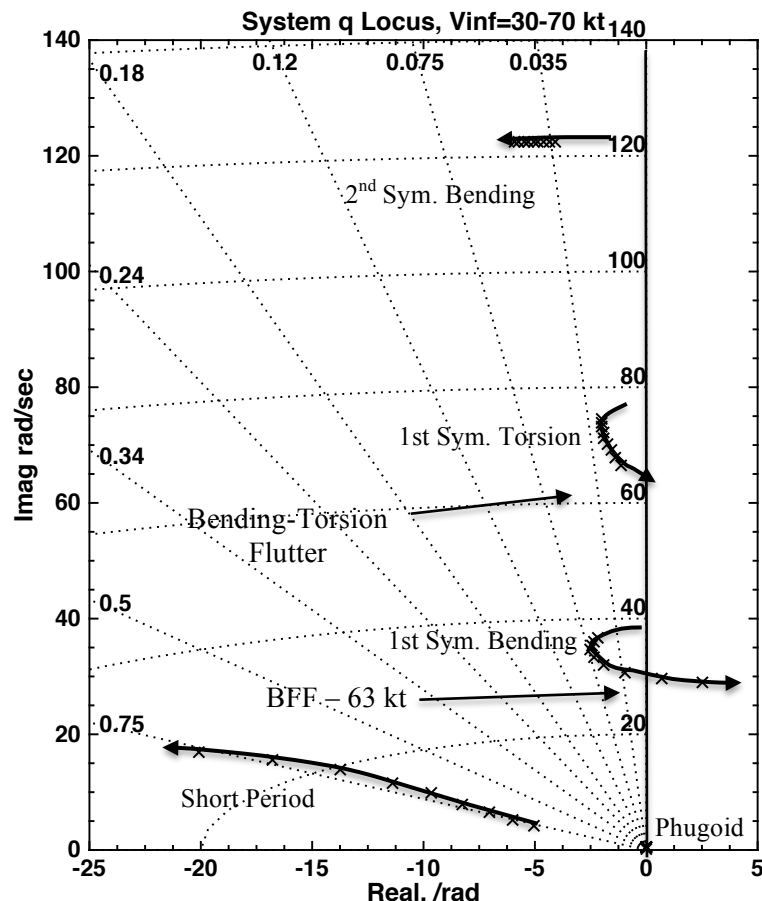
Figure 20, Dynamic-Pressure Root Locus – Flight-Dynamics Model

American Institute of Aeronautics and Astronautics

involving the first-bending and first-torsion modes. This flutter condition, as modeled, occurs at a flight velocity above 70 kt, with a flutter frequency of about 9.7 Hz.

Finally, consider the branch labeled "2nd Sym. Bending. This branch begins near the imaginary axis at 145.6 rad/sec, this mode's vibration frequency, and as the flight velocity increases, these roots simply move further into the left half plane. The phugoid roots remain near the origin at all flight velocities.

Neither truncation nor residualization of this third elastic degree of freedom alone had a major effect on the flutter results. The main result was slight modifications of the damping ratios of the retained aeroelastic modes, while only slightly affecting the flutter speeds. The conclusion here is that this third elastic degree of freedom has a small effect on the dynamics and the flutter characteristics.

However, as in [1], truncation or residualization of both the second and third elastic degrees of freedom leads to quite different results. With a truncated model the "Short-Period" and "1st-bending" modes appear to interact much less in the absence of the "1st Torsion" mode, having a q locus similar to that of a rigid model. In contrast, the q root locus for the residualized model is quite similar to that for the full-order model. There again exists considerable interaction between the "Short-Period" and "1st Bending" modes, and this residualized model also suggests BFF occurs at a flight velocity close to 63 kt. These combined results indicate that the static-elastic effects of the first-torsion mode, included in the residualized model, are important to the existence of BFF here.

C. Flutter-Results Comparisons

In addition to comparing these two sets of results (from the NASTRAN and FD Models), we have also compared the flutter results with those from three other models, plus those obtained in flight test. Two of these other models are described in [16], and are based on high-fidelity computation fluid dynamics and computational structural mechanics (CFD/CSM) modeling techniques. The third additional model was developed using ZAERO [17], another commercially available code.

The summary of this comparison is presented in Table 3. The entries in the left column refer to the version of the FEM used in the analysis, and the difference between these FEMs include differences in mass properties and/or wing construction. So all these results do not correspond to the same vehicle, and all should not agree. But they should agree when considering the same vehicle or FEM. The shaded rows include the results already discussed, plus the flight-test results. These results generally agree rather well, and the differences between the flight-test and model results continue to be investigated.

The results for the other FEMs all agree quite well, with the possible exception of those obtained from the CFD/CSM model for the FEM 1.1. It is hypotthsized that this difference is more due to the extraction of the

Table 3, Comparison of Flutter Results From Several Sources

Model Version	Dynamic Model	Flutter Speed, kt	Flutter Frequency, Hz
FEM 2.1 WS 1	MSC/NASTRAN (VT)	63.6	5.1
FEM 2.1 WS 1	Flight Dynamics (S&A)	63.0	4.8
Flight Article (FEM 2.1)	Flight Test (UMN)	58.3	4.0
FEM 1.1 WS 1 Aft cg	CFD/CSD (CMSoft)	71.4	3.5
FEM 1.1 WS 1 Aft cg	IOROM (STI)	61.5	4.3
FEM 1.1 WS 1 Aft cg	MSC/NASTRAN (VT)	61.1	3.9
FEM 1.1 WS 1 Aft cg	ZAERO (VT)	62.1	3.6
FEM 1.1 WS 1 Aft cg	Flight Dynamics (S&A)	60.1	3.5
FEM 3.3 WS 2 (flex)	CFD/CSD (CMSoft)	59.8	4.2
FEM 3.3 WS 2 (flex)	MSC/NASTRAN (VT)	57.3	4.0
FEM 3.3 WS 2 (flex)	Flight Dynamics (S&A)	56.5	3.7

flutter speed and frequency from a non-linear time simulation, rather than from basic differences between the models. Plus, since the IOROM model is derived from the CFD/CSM model, and that the IOROM results agree with NASTRAN, ZAERO, and the FD Model seems to support this hypothesis. The degree with which the results from the FD model agree with results from the other more established and/or more powerful is quite surprise. Plus, the Flight-Dynamics model ignores the effects of unsteady aerodynamics, which all the other models include. So it would appear that unsteady effects are negligible, with regard to BFF predictions.

VIII. Concluding Remarks

A relatively low order linear, semi-analytical flight-dynamics model was developed to characterize the longitudinal dynamics of a flexible flying-wing research drone aircraft. A review of the equations of motion was presented, and the rigid-body degrees of freedom were defined in terms of the motion of the vehicle-fixed coordinate frame (mean axes), as required for flight-dynamics analysis. The analytical modeling utilized the free-vibration solution for the vehicle structure obtained from a NASTRAN finite-element model. The rigid-body aerodynamic coefficients were obtained using a vortex-lattice code, and the aeroelastic stability derivatives were derived from virtual-work concepts and vortex-lattice aerodynamics. All numerical analyses, except for NASTRAN, were performed in MATLAB[®]. The state variables used in the Flight-Dynamics model includes the same as those used in modeling a rigid vehicle, plus additional states associated with the elastic degrees of freedom. This model structure helped to provide insight and transparency in the modeling and in the interpretation of results.

The second symmetric vibration mode appears to be an important contributor to body-freedom flutter. As modeled, the longitudinal dynamics of the vehicle are characterized by a slightly unstable phugoid mode, a well-damped, pitch-dominated, elastic-short-period mode, and three coupled aeroelastic modes. The elastic-short-period and aeroelastic modes involve significant coupling between the rigid-body and elastic degrees of freedom, as indicated by their mode shapes, and this coupling leads to the BFF condition.

It was shown that in spite of the model's relative simplicity, the body-freedom and bending-torsion flutter speeds, frequencies, and genesis modes suggested by this model agreed quite well with the analytical predictions from flight test-results and several other well-established models, including NASTRAN. Plus, the transient response agreed with measured flight-test responses as well, thus providing additional validations. Is clear from these results that this vehicle is quite flexible, with quick attitude response. And the effects of flexibility make the pitch response even faster.

IX. Acknowledgements

X. Appendices

Appendix A - Vehicle Data

Table A1, Comparison of FEM and Ground-Test Mass Properties

Property	FEM	Test	Diff. with FEM
Mass, lbs	14.77	14.74	0.22%
X cg, from nose, in	23.54	23.73	-0.79%
Ixx, lbs-in^2	10816.18	10687.93	1.20%
Iyy, lbs-in^2	1845.37	1804.00	2.29%

Table A2, Planform Parameters

Planform Area, S	Span, b	Aspect Ratio, AR	Taper Ratio, λ	M.A.C., $\overline{c}$	LE Sweep, Λ_{LE}
11.55 ft^2	10 ft	8.66	0.285	1.3 ft	22 deg

Appendix B - Aerodynamic and Aeroelastic Coefficient Data

Table B1, Rigid-Body Longitudinal Stability Derivatives

C_{L_α} /rad	C_{M_α} /rad	C_{L_q} sec	C_{M_q} sec	$C_{L_{\delta_1}}$ /rad	$C_{M_{\delta_1}}$ /rad
4.592	-0.164	4.424	-1.876	0.794	0.021
$C_{L_{\delta_2}}$ /rad	$C_{M_{\delta_2}}$ /rad	$C_{L_{\delta_3}}$ /rad	$C_{M_{\delta_3}}$ /rad	$C_{L_{\delta_4}}$ /rad	$C_{M_{\delta_4}}$ /rad
0.603	-0.050	0.506	-0.202	0.416	-0.302
C_{D_α} /rad	$C_{D_{\delta_1}}$ /rad	$C_{D_{\delta_2}}$ /rad	$C_{D_{\delta_3}}$ /rad	$C_{D_{\delta_4}}$ /rad	
0.077	0.0200	0.0056	0.0065	0.0075	

Table B2, Aeroelastic Coefficients (all /rad, unless otherwise noted)

$C_{L_{\eta_1}}$	$C_{L_{\dot\eta_1}} V_\infty$ (ft)	$C_{M_{\eta_1}}$	$C_{M_{\dot\eta_1}} V_\infty$ (ft)	$C_{Q_{1\alpha}}$	$C_{Q_{1q}} V_\infty$ (ft)	$C_{Q_{1\delta_1}}$	$C_{Q_{1\delta_2}}$
-1.515	0.271	-0.0138	-0.502	-0.508	-0.440	0.093	0.073
$C_{Q_{1\delta_3}}$	$C_{Q_{1\delta_4}}$	$C_{Q_{1\eta_1}}$	$C_{Q_{1\eta_2}}$	$C_{Q_{1\eta_3}}$	$C_{Q_{1\dot\eta_1}} V_\infty$ (ft)	$C_{Q_{1\dot\eta_2}} V_\infty$ (ft)	$C_{Q_{1\dot\eta_3}} V_\infty$ (ft)
-0.008	-0.191	0.163	0.559	-0.015	-0.289	-0.022	0.156
$C_{L_{\eta_2}}$	$C_{L_{\dot\eta_2}} V_\infty$ (ft)	$C_{M_{\eta_2}}$	$C_{M_{\dot\eta_2}} V_\infty$ (ft)	$C_{Q_{2\alpha}}$	$C_{Q_{2q}} V_\infty$ (ft)	$C_{Q_{2\delta_1}}$	$C_{Q_{2\delta_2}}$
-1.434	0.348	-1.1107	-0.102	-0.466	-0.439	0.002	-0.055
$C_{Q_{2\delta_3}}$	$C_{Q_{2\delta_4}}$	$C_{Q_{2\eta_1}}$	$C_{Q_{2\eta_2}}$	$C_{Q_{2\eta_3}}$	$C_{Q_{2\dot\eta_1}} V_\infty$ (ft)	$C_{Q_{2\dot\eta_2}} V_\infty$ (ft)	$C_{Q_{2\dot\eta_3}} V_\infty$ (ft)
-0.086	-0.034	0.157	0.515	0.072	-0.110	-0.103	0.247
$C_{L_{\eta_3}}$	$C_{L_{\eta_3}} V_\infty$ (ft)	$C_{M_{\eta_3}}$	$C_{M_{\eta_3}} V_\infty$ (ft)	$C_{Q_{3\alpha}}$	$C_{Q_{3q}} V_\infty$ (ft)	$C_{Q_{3\delta_1}}$	$C_{Q_{3\delta_2}}$
0.270	-0.651	0.2326	0.408	0.578	0.316	-0.100	0.002
$C_{Q_{3\delta_3}}$	$C_{Q_{3\delta_4}}$	$C_{Q_{3\eta_1}}$	$C_{Q_{3\eta_2}}$	$C_{Q_{3\eta_3}}$	$C_{Q_{3\dot\eta_1}} V_\infty$ (ft)	$C_{Q_{3\dot\eta_2}} V_\infty$ (ft)	$C_{Q_{3\dot\eta_3}} V_\infty$ (ft)
0.198	0.159	-0.191	-0.518	-0.058	0.117	0.106	-0.316

Table B3, Static-Elastically Adjusted Aerodynamic Coefficients

C_{L_α} /rad	C_{M_α} /rad	C_{L_q} sec	C_{M_q} sec	$C_{L_{\delta_1}}$ /rad	$C_{M_{\delta_1}}$ /rad
6.02	-0.418	6.46	-2.26	0.598	0.034
$C_{L_{\delta_2}}$ /rad	$C_{M_{\delta_2}}$ /rad	$C_{L_{\delta_3}}$ /rad	$C_{M_{\delta_3}}$ /rad	$C_{L_{\delta_4}}$ /rad	$C_{M_{\delta_4}}$ /rad
0.494	-0.061	0.595	-0.234	0.841	-0.342
C_{D_α} /rad	$C_{D_{\delta_1}}$ /rad	$C_{D_{\delta_2}}$ /rad	$C_{D_{\delta_3}}$ /rad	$C_{D_{\delta_4}}$ /rad	
0.110	0.0200	0.0056	0.0065	0.0075	

Xi. References

1. Schmidt, D.K. "MATLAB®-Based Flight-Dynamics and Flutter Modeling of an Unmanned Flying-Wing Research Drone," to Appear in the *Journal of Aircraft.*
2. *MSC/NASTRAN Quick Reference Guide: version 68*. MacNeal-Schwendler Company, 2013.

3. Schmidt, David K., *Modern Flight Dynamics,* McGraw-Hill, 2012.
4. Bisplinghoff, R. L., Ashley, H., *Principles of Aeroelasticity*. John Wiley & Sons, Inc., New York, 1962.
5. Yates, E. C., Jr., "Calculation of Flutter Characteristics for Finite-Span Swept or Unswept Wings at Subsonic and Supersonic Speeds by a Modified Strip Analysis," NACA RML57L10, 1958.
6. Schmidt, D.K., "Discussion: The Lure of the Mean Axes," *Journal of Applied Mechanics,* Dec. 2015**, 82**(12). doi: 10.1115/1.4031567
7. Dusto, A. R., et al, "A Method for Predicting the Stability Characteristics of an Elastic Airplane," Vol. 1-FLEXSTAB Theoretical Description," NASA Report No. CR-114712, 1974.
8. Waszak, M. and Schmidt, D.K., "Flight Dynamics of Aeroelastic Vehicles," *Journal of Aircraft,* Vol. 25, No. 6, June 1988.
9. Milne, R.D., *Dynamics of the Deformable Aeroplane,* British Aeronautical Research Council, London, Reports & Memoranda 3395, 1964.
10. Buttrill, C.S., Zeiler, T.A., and Arbuckle, P.D., "Nonlinear Simulation of a Flexible Aircraft in Maneuvering Flight," AIAA Paper 87-2501-CP. AIAA Flight Simulation Technologies Conference (Monterey, CA), August 1987.
11. Regan, C, and Taylor, B., "mAEWing1: Design, Build, Test," Proceedings of the AIAA SciTech Conference, San Diego, CA, Jan. 4-8, 2016.
12. Burnett, E.L., Atkinson, C., Beranek, J., Sibbitt, B., Holm-Hansen, B., and Nicolai, L., " NDOF Simulation Model for Flight Control Development with Flight Test Correlation," Lockheed Martin Aeronautics Co., AIAA Paper No. 2010-7780, Toronto, August 2010.
13. Melin, T., *A Vortex Lattice MATLAB Implementation for Linear Aerodynamic Wing Applications,* Dept. of Aeronautics, Royal Institute of Technology, Sweden, Dec., 2000.
14. Pfifer, H., and Danowsky, B., "System Identification of a Small Flexible Aircraft," Proceeding, AIAA SciTech Conference, Sand Diego, CA, Jan. 4-8, 2016.
15. Rodden, W. P., and Johnson, E. H., *MSC/NASTRAN Aeroelastic Analysis: User's Guide; Version 68*. MacNeal-Schwendler Corporation, 1994.
16. Danowsky, B., Lieu, T., and Coderre-Chabot, A., "Control Oriented Aeroservoelastic Modeling of a Small Flexible Aircraft using Computational Fluid Dynamics and Computational Structural Dynamics." Proceedings of the AIAA SciTech Conference, San Diego, CA, Jan. 4-8, 2016.
17. *ZAERO Theoretical Manual*, ZONA Technology Inc., ZONA 02 -12.4, Scottsdale, AZ, 2011.

American Institute of Aeronautics and Astronautics